Phys Chem Minerals (2002) 29: 98–111
DOI 10.1007/s002690100205

ORIGINAL PAPER

N. R. Khisina · R. Wirth

Hydrous olivine $(Mg_{1-y}Fe^{2+}_{y})_{2-x}v_{x}SiO_{4}H_{2x}$ – a new DHMS phase of variable composition observed as nanometer-sized precipitations in mantle olivine

Received: 15 January 2001 / Accepted: 2 July 2001

Abstract An olivine grain from a peridotite nodule 9206 (Udachnaya kimberlite, Siberia) was investigated by TEM methods including AEM, HRTEM, SAED and EELS techniques. A previous study of the 9206 olivine sample revealed OH absorption bands in the IR spectrum and abundant nanometer-sized OH-bearing inclusions, of hexagonal-like or lamellar shape. Inclusions, which are several hundred nm in size, consist of 10 Å phase, talc and serpentine (chrysotile and lizardite). The lamellar (LI) and hexagon-like small inclusions of several ten nm in size (SI) are the topic of the present paper. AEM investigations of the inclusions reveal Mg, Fe and Si as cations only. The Mg/Si and Fe/Si atomic ratios are lower in the inclusions than in the host olivine. The Si concentration in the olivine host and both lamellar inclusions and small inclusions is the same. A pre-peak at 528eV was observed in EEL spectra of LI and SI, which is attributed to OH^- or Fe^{3+}. From these data it is concluded that there is a OH^-- or Fe^{3+}-bearing cation-deficient olivine-like phase present.

HRTEM lattice fringe images of LI and SI exhibit modulated band-like contrasts, which are superimposed onto the olivine lattice. Diffraction patterns (Fourier-transforms) of the HREM images as well as SAED patterns show that the band-like contrasts in HRTEM images of the inclusions are caused by periodic modulations of the olivine lattice. Three kinds of superperiodicity in the olivine structure such as 2a, 3a and 3c, were observed in SAED patterns. The corresponding olivine supercells labelled here as Hy-2a, Hy-3a and Hy-3c were derived. The M1-vacancies located in the (100) and (001) octahedral layers of the olivine lattice are suggested to form ordered arrays of planar defects (PD), which cause the band-like contrasts in HRTEM patterns as well as the superperiodicity in the SAED patterns.

The vacancy concentrations as well as the chemical composition of Hy-2a, Hy-3a and Hy-3c olivine supercells were calculated using crystal chemical approaches, assuming either $\left\{(OH)^{\langle}_{O} - V''_{Me} - (OH)^{\langle}_{O}\right\}^{\leftrightarrow}$, or $\left\{Fe^{\langle}_{Fe} - H'_{Me}\right\}^{\leftrightarrow}$ or $\left\{2Fe^{\langle}_{Fe} - V''_{Me}\right\}^{\leftrightarrow}$ point defect associates. The calculated theoretical compositions $Mg_{1.615}Fe^{+2}{}_{0.135}v_{0.25}SiO_4H_{0.5}$ (Hy-2a) and $Mg_{1.54}Fe^{2+}{}_{0.12}v_{0.33}SiO_4H_{0.66}$ (Hy-3a and Hy-3c) are in a good agreement with the AEM data on inclusions. Hy-2a, Hy-3a and Hy-3c are considered to be a hydrous olivine with the extended chemical formula $(Mg_{1-y}Fe^{2+}{}_{y})_{2-x}v_xSiO_4H_{2x}$. The crystal structure of hydrous olivine is proposed to be a modular olivine structure with Mg-vacant modules. The crystal chemical formula of hydrous olivines in terms of a modular structure can be written as $[MgSiO_4H_2] \cdot 3[Mg_{1.82}Fe_{0.18}SiO_4]$ for Hy-2a, $[MgSiO_4H_2] \cdot 2[Mg_{1.82}Fe_{0.18}SiO_4]$ for Hy-3a and Hy-3c.

Hydrous olivine is suggested to be exsolved from the olivine 9206, which has been initially saturated by OH-bearing point defects. The olivine 9206 hydration as well as the following exsolution of hydrous olivine inclusions is suggested to occur at high pressure-high temperature conditions of the upper mantle.

Keywords Hydrous olivine · Ordered planar defects · OH^--bearing point defects · Transmission electron microscopy (TEM) · Hydrogen incorporation

Introduction

Water in the Earth mantle, its sources, transport and storage are the subject of controversial debate. The most common phases in the mantle, the α, β and γ phases of $(Mg, Fe)_2SiO_4$, are nominally anhydrous phases. How-

N. R. Khisina
Institute of Geochemistry and Analytical Chemistry
of Russian Academy of Science, Kosygin St. 19,
117975 Moscow, Russia
e-mail: urusov@geol.msu.ru

N. R. Khisina · R. Wirth (✉)
GeoForschungsZentrum Potsdam, Telegrafenberg C-120,
14473 Potsdam, Germany
e-mail: wirth@gfz-potsdam.de

ever, recent experiments have shown that they can carry large amounts of hydroxyl – up to 27 000 wt ppm H_2O under mantle conditions of 19.5 GPa and 1100 °C (Kohlstedt et al. 1996). There is another group of minerals, the so-called dense hydrous magnesium silicates (DHMS), which are also considered to be potential carriers of water in the mantle. However, the DHMS minerals such as phase A, phase B, phase D, phase F, superhydrous B, hydrous wadsleyite and hydrous ringwoodite (cf. Thompson 1992) have never been observed in natural rocks. Only the humite-like minerals, and the very recently reported 10-Å phase (Wirth and Khisina 1998; Khisina et al. 2001) are present in natural rocks. If we accept that most of the DHMS phases are absent in natural mantle rocks, because they have never been observed, the problem of carriers of hydroxyl in the mantle is focused on the hydrous α, β and γ phases of $(Mg, Fe)_2SiO_4$. Hydrous wadsleyite β-$Mg_{2-x}SiH_{2x}O_4$ with $0.00 \leq x \leq 0.25$ and hydrous ringwoodite γ-$Mg_{1.89}Si_{0.98}H_{0.3}0_4$ have been synthesised and investigated (Kudoh et al. 1996, 1999, 2000). From solubility experiments it is known that the maximum solubility of hydroxyl in olivine at the α–β phase boundary is 1200 wt ppm H_2O (Kohlstedt et al. 1996). This is much less than the maximum solubility of hydroxyl in the hydrous β and γ phases. In contrast to hydrous wadsleyite and hydrous ringwoodite, hydrous olivine has not been reported till now.

The question is, how is it possible that nominally anhydrous minerals can carry such large amounts of hydroxyl? Point-defect models are used to explain the presence of hydroxyl in the three different $(Mg, Fe)_2SiO_4$ phases (Beran and Putnis 1983; Bai and Kohlstedt 1993; Libowitzky and Beran 1995; Kohlstedt et al. 1996; Kudoh et al. 1996; Kudoh et Inoue 1999; Kudoh et al. 2000; Brodholt and Refson 2000; Mei and Kohlstedt 2000). Under anhydrous conditions metal vacancies and ferric iron on metal sites are the majority point defects (cf. references in Mei and Kohlstedt 2000). Under hydrous conditions, the concentrations of water-derived point defects may exceed those of metal vacancies. Consequently, water will affect the point-defect chemistry of olivine. There are three principal mechanisms that have to be considered as a mode of hydrogen incorporation in the $(Mg, Fe)_2\ SiO_4$ phases: interstitial, binding at cation vacancies and binding at silicon vacancies. Especially the binding at Si or Mg vacancies is discussed controversially. Si as well as M1 and M2 vacancies associated with OH are favoured in the model proposed by Libowitzky and Beran (1995). From a computer simulation study it was concluded that Si vacancies are energetically less favourable than Mg vacancies, therefore, water was expected to increase the number of Mg vacancies (Wright and Catlow 1994). Controversially, in a recent ab initio study (Brodholt and Refson 2000), the presence of protons was found to increase the number of Si vacancies. This is in contrast to dry olivine, where Si vacancies are many eV less favourable than Mg vacancies (Brodholt 1997). From experimental work it is concluded that metal vacancies are precisely the defects which are important for the incorporation of hydrogen in olivine (Bai and Kohlstedt 1993). Mei and Kohlstedt (2000) showed that ferric iron cations associated with metal vacancies could exceed the OH-bearing point-defect population. With increasing water fugacity the charge neutrality condition has been found to change from $[\mathrm{Fe}^{\langle\cdot}_{\mathrm{Me}}] = 2[V''_{\mathrm{Me}}]$ to $[\mathrm{Fe}^{\langle\cdot}_{\mathrm{Me}}] = [\mathrm{H}'_{\mathrm{Me}}]$ (Mei and Kohlstedt 2000).

Here we report that, additionally to hydrous wadsleyite and hydrous ringwoodite, hydrous olivine $(Mg_{1-y}Fe^{2+}_y)_{2-x}v_xSiO_4H_{2x}$ exists. Hydrous olivine was found as nanometer-sized inclusions in mantle olivine.

Description of the specimen and previous data

The investigated olivine grain (Fo_{82}) was taken from a peridotite nodule 9206 (kimberlite pipe Udachnaya, Siberia). A detailed description of the nodule is given in Khisina et al. (2000). The PT conditions derived from the nodule are 700–800 °C and 5.5–6 GPa (Ukhanov et al. 1988). IR spectra of olivine show OH absorption bands (Khisina et al. 2001). TEM examination of the olivine 9206 has revealed nanometer-sized OH-bearing inclusions: (1) lamellar inclusions of several 10 nm in width, (2) small inclusions up to several 10 nm in size, and (3) large inclusions up to several 100 nm in size. The large inclusions consist of 10-Å phase, talc and serpentine (chrysotile and lizardite), while hydrous olivine $Mg_{2-x}v_xSiO_4H_{2x}$ has been proposed as a possible phase in both small and lamellar inclusions. The large inclusions have been described in a previous paper (Khisina et al. 2001). The lamellar inclusions and small inclusions are the topic of the present paper. The specimen was thinned by conventional ion-beam thinning and lightly coated with carbon. The olivine single crystal [(0 1 0) foil] of olivine was investigated by transmission electron microscopy (TEM), analytical electron microscopy (AEM), electron energy-loss spectroscopy (EELS) and selected area electron diffraction (SAED).

TEM was carried out in a Philips CM200 electron microscope with an LaB_6 filament. AEM was performed using an EDAX X-ray analyser with ultrathin window. A Gatan image-filtering system GIF was used for EELS spectroscopy and for acquiring energy-filtered images. A detailed description of the TEM techniques is given in Khisina et al. (2000).

Results

TEM observations

Bright-field TEM images of the (0 1 0) olivine foil show arrays of precipitates, which are arranged parallel to either (1 0 0), or (1 0 2) or (1 0 $\bar{2}$) of the olivine matrix. The precipitates consist of three different types of inclusions: lamellar inclusions (LI), small inclusions (SI) and large inclusions. The lamellar inclusions are several 10 nm wide and about several micron long (Fig. 1a). They are oriented parallel to either (1 0 0) or (1 0 2) or (1 0 $\bar{2}$) of the olivine matrix. The small inclusions are up to several 10 nm and the large inclusions are up to several 100 nm in size. Both small and large inclusions show a hexagon-like shape (Fig. 1b, c). Arrows in Fig. 1b indicate some large inclusions; such inclusions

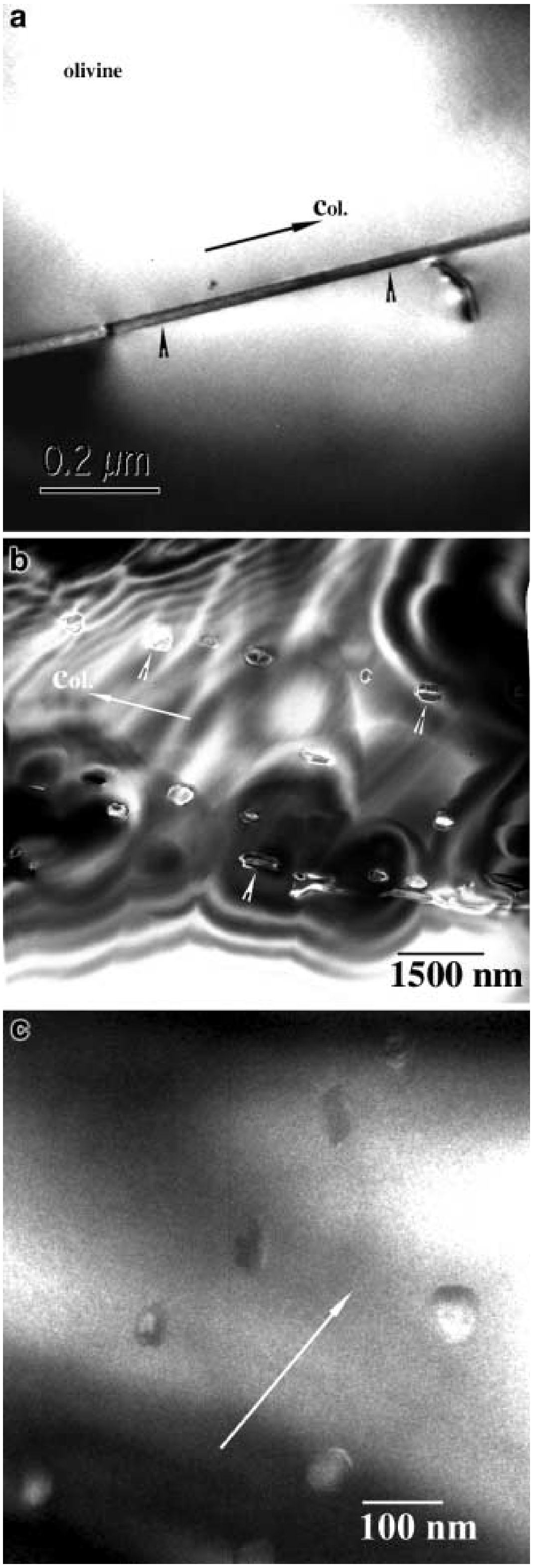

Fig. 1a–c Bright-field electron micrographs of inclusions in olivine sample 9206. (0 1 0) olivine foil. **a** Lamellar inclusion (LI) oriented parallel to (1 0 0) of the olivine matrix. *Small arrow heads* indicate the location of the inclusion. **b** Arrays of inclusions arranged along the *c* direction of the olivine matrix. The largest of inclusions (*arrow heads*) are composed by 10-Å-phase + talc + serpentine. **c** Arrays of small inclusions (SI) arranged along the [0 0 1] direction of the olivine matrix

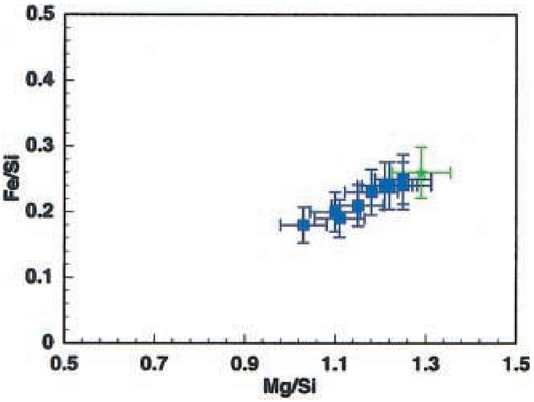

Fig. 2 Fe/Si net intensity ratio plotted versus Mg/Si net intensity ratio (cf. text). *Rectangles* indicate inclusions; host olivine (in green). The plot shows that both Mg and Fe decrease in inclusions with respect to the olivine matrix

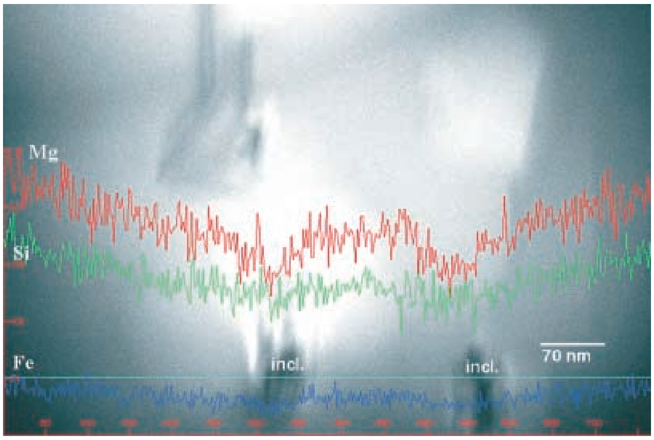

Fig. 3 Concentration profile across two inclusions in the olivine matrix. A thin straight line in the lower part of the image indicates the location of the line-scan. The *scan lines* show that the Mg and Fe concentrations in the inclusions decrease with respect to the olivine matrix while the Si concentration remains almost the same as in olivine (Si concentration does not increase)

consist of 10-Å-phase, serpentine and talc (Khisina et al., in press). Both small and large inclusions are arranged parallel to the lamellar inclusions (Fig. 1b, c).

The AEM analyses of LI and SI show only Mg, Fe and Si as cations. The Mg/Si net intensity ratio as well as the Fe/Si net intensity ratio is smaller in the lamellar precipitates and the small inclusions than in the host olivine (Fig. 2). This indicates that either the Si concentration in SI and LI is larger than in the olivine, or the Mg and Fe concentrations in SI and LI are lower than in the olivine. Concentration profiles across olivine and inclusions do not reveal any increasing of Si concentration in inclusions compared to the olivine host, while the Mg and Fe concentrations appear to decrease in LI and SI compared to that of the olivine host; a typical concentration profile is presented in Fig. 3. The oxygen K-edge of olivine in the EEL spectrum (Fig. 4a) does not show a prepeak at about 528 eV, which can be attributed to OH or Fe^{3+} according to Wirth (1997) and van Aken et al. (1998). However, this prepeak is observed in EEL spectra of lamellar inclusions and small inclusions (Fig. 4b).

Energy-filtered HRTEM lattice-fringe images of lamellar inclusions and small inclusions exhibit coherent olivine/LI and olivine/SI interfaces (Figs. 5, 6). The (2 0 0) and (0 0 2) lattice fringes are resolved in the olivine matrix as well as in lamellar inclusions and the small inclusions (Figs. 5, 6).

The lamellar inclusion in Fig. 5 and the small inclusion in Fig. 6 show a modulated contrast pattern, a band-like pattern, which is superimposed onto the olivine lattice-fringe pattern (Figs. 5a, b, e and 6a). Band-like contrasts of distinct kinds were observed in HRTEM lattice-fringe images of both LI and SI. Periodic band-like contrasts observed parallel to (1 0 0) exhibit spacings corresponding to every second (Fig. 5a, b, e) or every third olivine unit cell. Additionally, periodic band-like contrasts parallel to (1 0 1) (Fig. 6a) or (1 0 2) (Fig. 5a, b) were observed; in the latter case, the HRTEM lattice fringe images show a combination of (1 0 2) and (1 0 0) band-like contrasts. The modulated contrast observed in Figs. 5 and 6 disappears within seconds due to electron irradiation damage, thus indicating that the LI and SI are not stable under the elec-

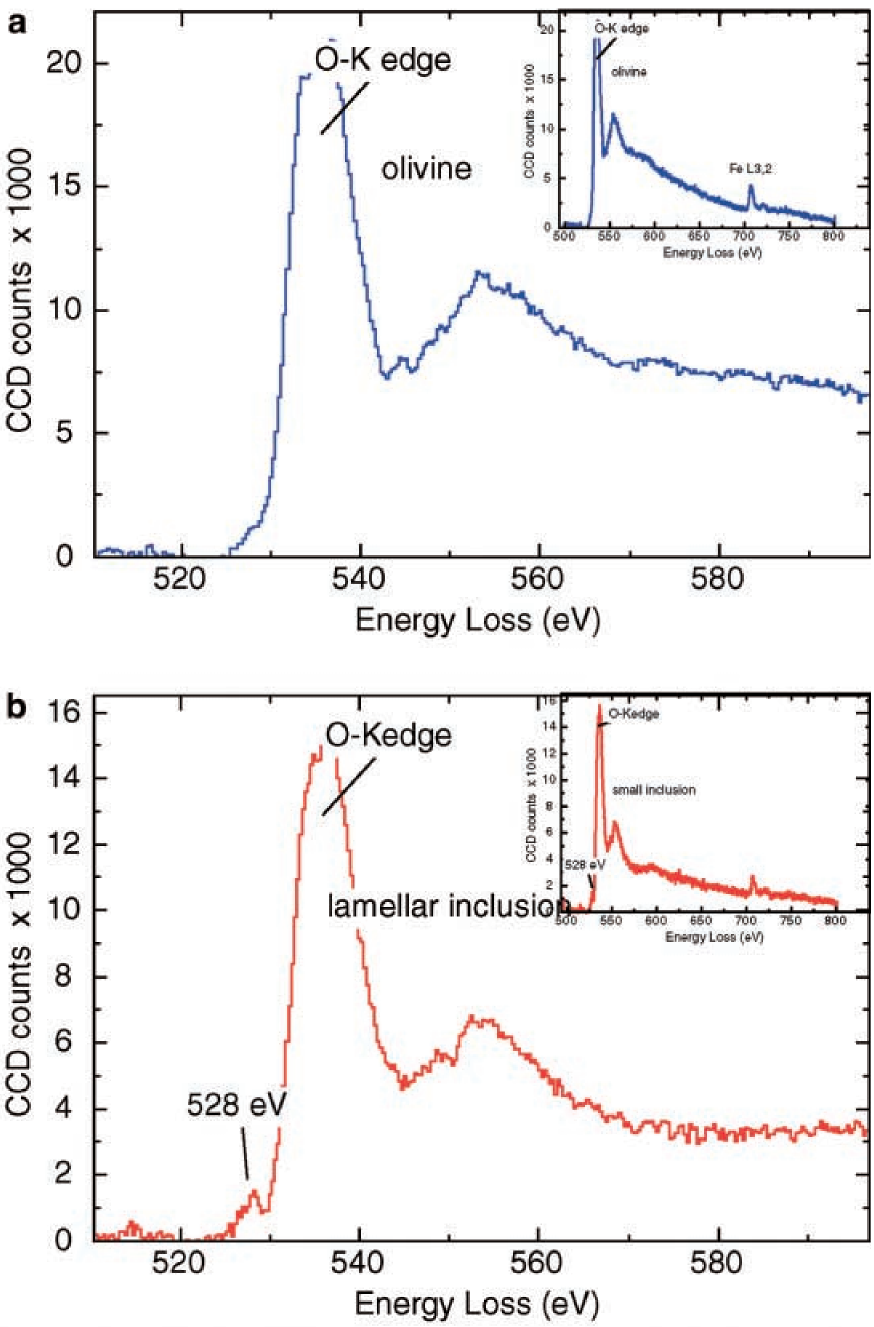

Fig. 4a, b EEL spectra from the olivine matrix **a** and from an inclusion **b**. The prepeak at 528 eV observed in **b** indicates that water is present in the inclusion. In the EEL spectrum from the olivine matrix **a** the prepeak at 528 eV is absent. The Fe L3, 2 peak indicative for Fe is observed at about 709 eV in both spectra tron beam. Once the modulations have disappeared, only the olivine lattice fringes are observed in LI and SI (the region framed and labelled A in Fig. 5a; upper right and lower left corner in Fig. 5b).

Diffraction patterns (fast Fourier transforms, FFT) from high-resolution images also reveal a superperiodicity (Figs. 5c, f and 6b). The $3d_{101}$ superperiodicity in [1 0 1]* reciprocal direction of olivine is shown in

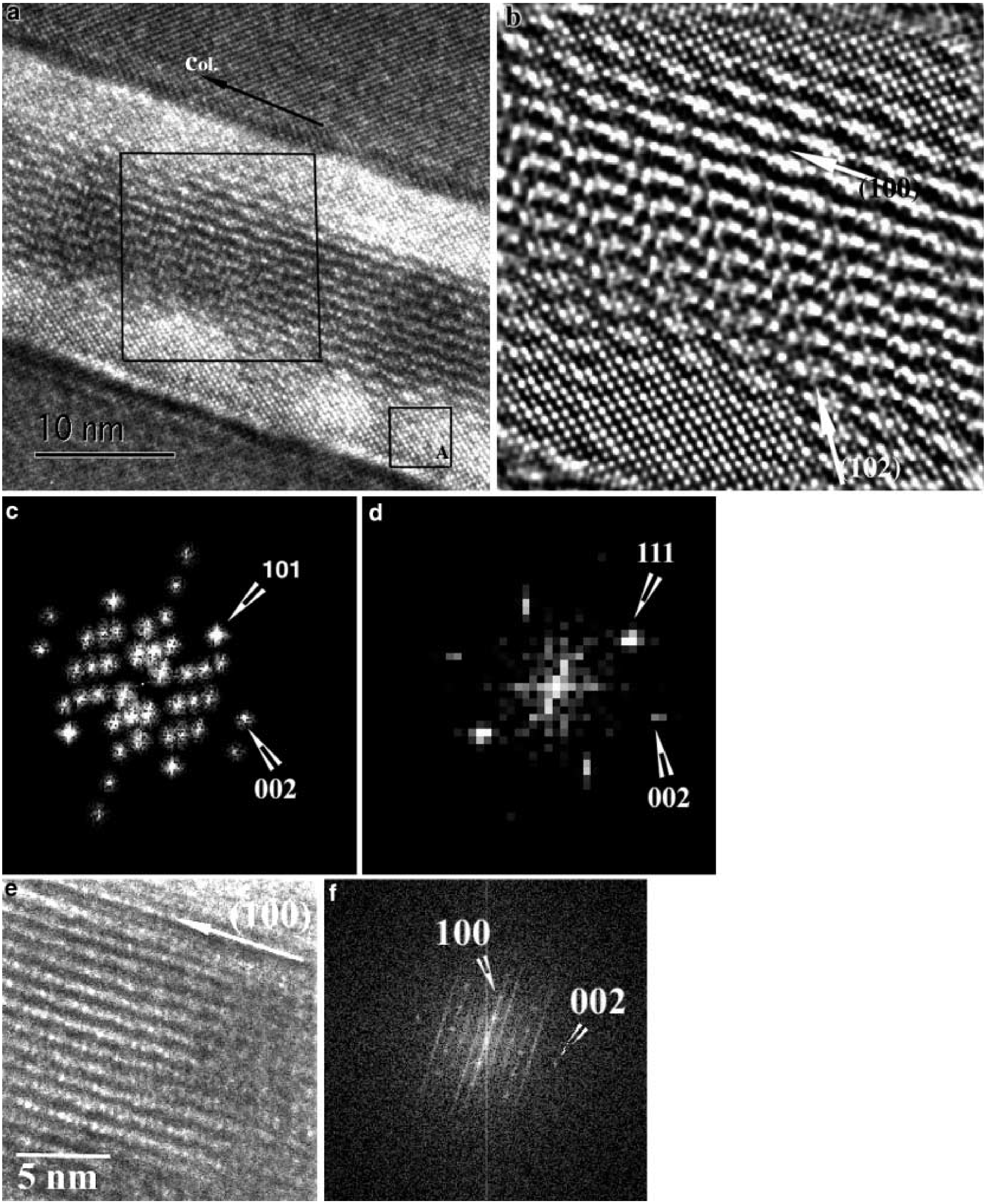

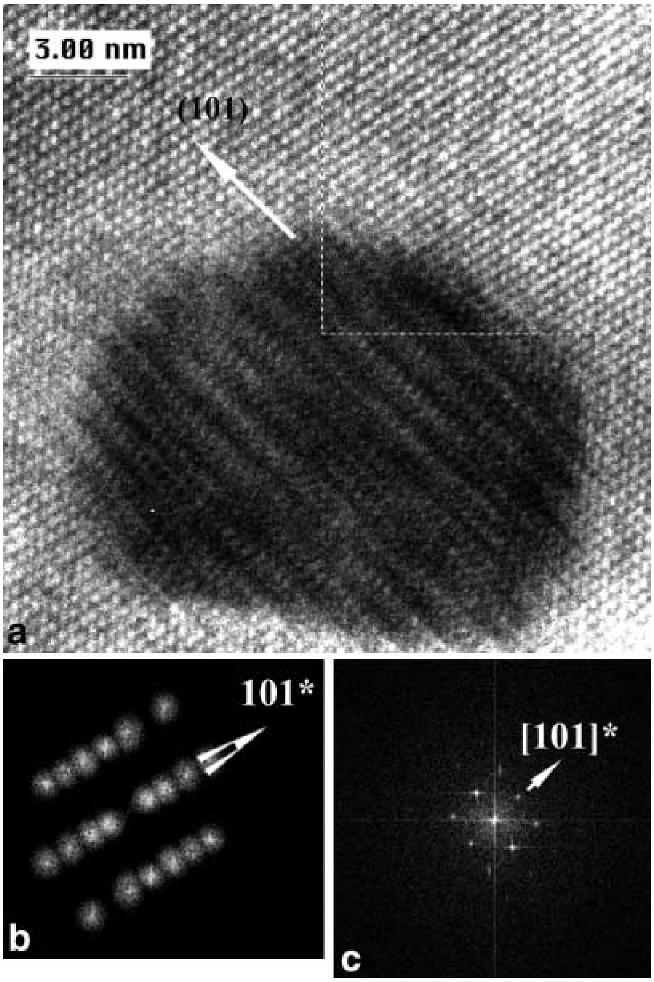

Fig. 6a–c Energy-filtered HRTEM lattice-fringe images of one of the small inclusions (SI). (0 1 0) olivine foil. **a** A periodic band-like contrast is observed parallel to (1 0 1). **b** The diffraction pattern (Fourier transform) from the image in **a** shows the $3d_{101}$-superperiodicity along [1 0 1]* direction of the reciprocal lattice of olivine. **c** Diffraction pattern (Fourier transform) from the olivine matrix in the vicinity of the inclusion

Fig. 6b. The $2d_{100}$ and $8d_{102}$ superperiodicities are observed in Fig. 5c. In addition to the $2d_{100}$ superperiodicity, streaks with a spacing of $3d_{001}$ are observed along the a^* direction in Fig. 5f. Very weak superspots which are not visible in the image (Fig. 5f) form the $3d_{100}$ superperiodicity in the a^* direction.

SAED patterns support the idea that the band-like contrasts in HRTEM lattice-fringe images (Figs. 5a, b, e and 6a) are caused by periodic modulations of the olivine lattice. The SAED patterns of some of the inclusions exhibit a superperiodicity along [100]* or [001]* directions of the olivine reciprocal lattice (Fig. 7a, b); both the direction and the spacing of the superperiodicity in the SAED patterns are consistent with these of FFT patterns shown in Fig. 6b. Three different kinds of superperiodicities were observed in the SAED patterns (Fig. 7a–d). Consequently, three olivine supercells, derived from the Pbnm olivine unit-cell geometry, were determined: Hy-3c, Hy-3a and Hy-2a (Table 1). This terminology uses Hy for hydrous olivine; 3c-, 3a- and 2a-indicate both the direction and the spacing of superperiodicity.

In SAED patterns of Hy-3c (Fig. 7a) and Hy-3a (Fig. 7b) the spots with $h_{\mathrm{Hy}} + l_{\mathrm{Hy}} = 2n + 1$ are absent. This indicates that the olivine unit cell and the supercell of olivine have the same symmetry Pbnm. The only difference is that the translation *n* which is 1/2 a + 1/2 c in the olivine unit cell, is replaced by 3/2 a + 3/2 c in the olivine supercell. However, in SAED patterns of Hy-2a, Hy-$3d_{101}$ and Hy-$8d_{102}$ reflections with $h_{\mathrm{Hy}} + l_{\mathrm{Hy}} = 2n + 1$ are observed. This means that the symmetry of these supercells is reduced with respect to the olivine unit cell (Table 1).

Crystal chemical approaches

Periodic array of planar defects

The observed superperiodicity in the SAED patterns is the key to understanding the nature of the lamellar (LI) and the small inclusions (SI). In general, superperiodicity implies that atomic planes of a given topology, which is crystal-chemically equivalent in a basic lattice, become nonequivalent due to ordering of cations or vacancies. Cations or vacancies can create a superperiodicity in the diffraction pattern if they are arranged in only one and the same sublattice of the crystal structure. In the olivine structure there are M1 and M2 octahedral sites, which are occupied by Mg and Fe, as well as tetrahedral sites occupied by Si. We exclude a cation ordering from the present consideration because Fe and Mg in the olivine structure is well known to be completely disordered. Therefore, either metal or Si vacancies are responsible for the observed superperiodicity in LI and SI. According to the AEM data, the Mg/Si and Fe/Si ratios decrease in LI and SI with respect to olivine (Fig. 2), thus indicating that the olivine supercells described above will contain metal vacancies. Consequently, the

◀

Fig. 5a–f Energy-filtered HRTEM lattice fringe images of the lamellar inclusion shown in Fig. 1a. (0 1 0) olivine foil. **b** Enlarged image of the centre region of the lamellae (large frame, **a**. *Arrows* are oriented parallel to (1 0 2) and (1 0 0) planes of the olivine lattice. The complicated contrast pattern observed in **a** and **b** consists of two systems of periodic band-like contrasts, one of them with a spacing of $2d_{100}$ parallel to (1 0 0) of olivine; the other is $8d_{102}$-spaced and parallel to (1 0 2) of olivine. The regions with irradiation damage (labelled *A* in **a** and observed in the *lower left corner* in **b**) show the olivine lattice fringes only without the periodic band-like contrast. **c** Diffraction pattern (Fourier transform) from the area with the band-like contrasts (*frame* **a**). In addition to the olivine spots, superspots are observed. **d** Diffraction pattern (Fourier transform) from the area labelled *A* in **a**. The pattern shows the olivine spots only. 101* and 002* olivine spots are indicated in **c** and **d**. **e, f**. Another part of the lamellar inclusion shown in Fig. 1a. **e** Periodic band-like contrasts, which are parallel to (1 0 0) of olivine and **f** the corresponding diffraction pattern (Fourier transform)

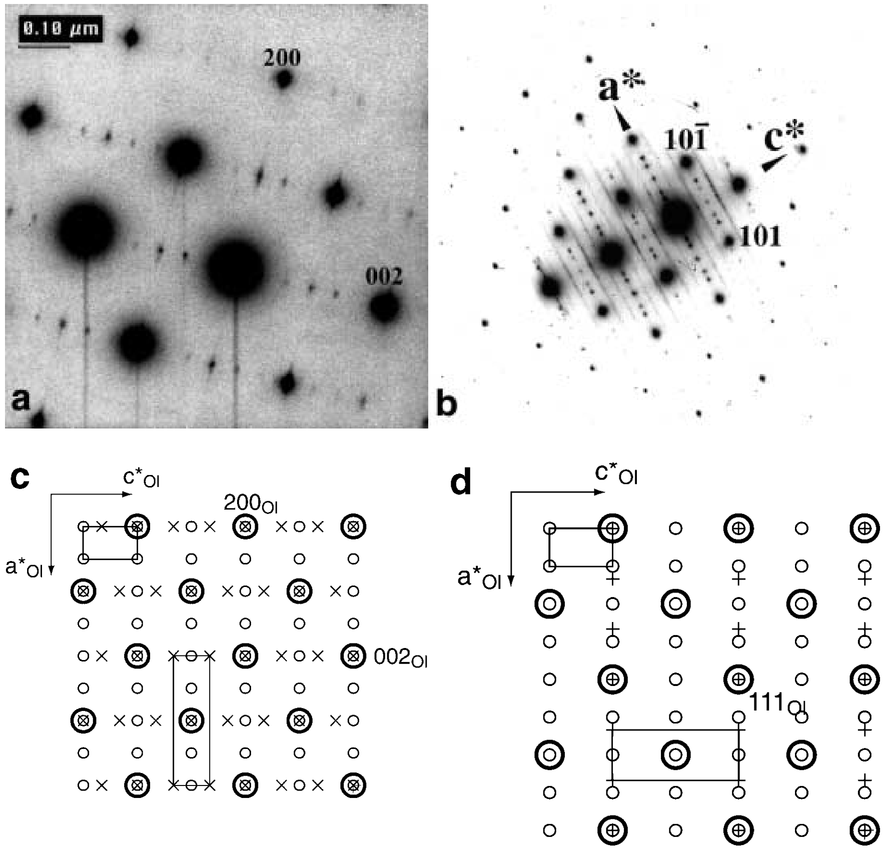

Fig. 7a–d SAED patterns of inclusions with a periodic band-like contrasts; (0 1 0) olivine zone axis. **a** Energy-filtered SAED pattern from an inclusion with 3c-superperiodicity of the olivine lattice. Weak superspots are observed along the c^* direction of olivine. These spots form the electron diffraction pattern, which is superimposed onto the olivine reciprocal lattice; such a schematic pattern with symbols is given in **c**. The olivine spots with $h + l = 2n + 1$, which are forbidden in the space group Pbnm of the olivine lattice, are observed here because the symmetry of the basic olivine cell is reduced due to the presence of ordered M1-vacant planar defects (cf. text). *Vertical streaks* observed in **a** are artefacts produced by the CCD camera because of the high dynamic range between the strong and the weak spots. **b** Superposition of an electron diffraction pattern from coexisting areas with 2a- and 3a-olivine superperiodicity. *Continuous streaks* observed along a^* of olivine correspond to a 3c supercell, which is disordered here, in contrast to the ordered 3c supercell in **a**. Notice the splitting of the spots from the 2a supercell. This splitting is due to the reduced symmetry of the 2a supercells twinned now by (1 0 0). The beta angle in the 2a supercell in **b** is slightly less than 90°. **c** and **d** show schematically the olivine reciprocal lattice together with the superspots observed in **a** and **b**. *Large circles* Olivine; *small open circles* the spots of the 2a supercell of olivine; *crosses* (+) the spots of the 3a supercell of olivine; *crosses* (x) the spots of the 3c supercell of olivine. **c** A superposition of olivine spots and the spots of Hy-2a and Hy-3c superlattices. The Hy-2a unit cell is framed in the *upper left corner*; the Hy-3c unit cell is framed *at the bottom*. **d** A superposition of olivine spots and the spots of Hy-2a and Hy-3a superlattices. The Hy-2a unit cell is framed in the *upper left corner*, the Hy-3a unit supercell is framed *at the bottom*. The drawing **d** corresponds to the SAED pattern in **b**. The *streaks* along a^* as well as the *splitting of the spots* of 2a supercell are ignored in **d**

ordering of metal vacancies in either M1 or M2 will result in the formation of supercells, which are observed in the diffraction patterns. We suggest the vacancies to be M1 vacancies; for energetic reasons they can be more easily created than M2 vacancies (Lasaga 1981; Brodholt 1997). The M1 vacancies located in the (1 0 0) and (0 0 1) octahedral layers of the olivine lattice are considered to form planar defects (PD). These PD are causing the band-like contrasts which are observed in HRTEM lattice-fringe images (Figs. 5, 6).

M1-vacancy concentrations

The olivine superstructure spots observed in SAED patterns of SI and LI as well as HRTEM data indicate a regular array of planar defects with distinct spacings. However, the vacancy density and the vacancy arrangement within an individual PD and between PD are unknown. Generally, planar defects can be either fully or partially free of metal ions in M1; they can be either continuous or discontinuous; a structure of individual PD can be ordered or disordered; they can be ordered or disordered related to each other. The arrangement of the planar defects and/or that of the vacancies within the planar defects can be deduced from the electron diffraction pattern. Comparing the general considerations with the diffraction data, three cases of a regular array of planar defects can be derived. (1) M1 sites in PD are fully vacant; as a result, sharp superspots should appear in the diffraction pattern; (2) half of the M1 sites are vacant and the other half is occupied, forming a vacancy-ordered PD

Table 1 Olivine superstructures observed in small (SI) and lamellar (LI) inclusions

Olivine superstructure (Hy)	HRTEM data		SAED data
	Periodic planar defects		Olivine superstructure
	Orientation	Periodicity	Unit supercell parameters
Hy-2a	(1 0 0)	9.5 Å = $2a_{ol}$	$a_{Hy} = 2a_{ol} = 9.5\,Å$ $b_{Hy} = b_{ol} = 10.2\,Å^{a}$ $c_{Hy} = c_{ol} = 6\,Å$ $V_{Hy} = 2V_{ol} = 582\,Å^{3}$ $Z = 8$ S.G. P11m or P1 No forbidden spots
Hy-3a	(1 0 0)	7.1 Å = $3/2a_{ol}$	$A_{Hy} = 3a_{ol} = 14.2\,Å$ $B_{Hy} = b_{ol} = 10.2\,Å^{a}$ $C_{Hy} = c_{ol} = 6\,Å$ $V_{Hy} = 3V_{ol} = 873\,Å^{3}$ $Z = 12$ S.G. Pbnm $h_{Hy} + l_{Hy} \neq 2n + 1$
Hy-3c	(0 0 1)	9 Å = $3/2c_{ol}$	$a_{Hy} = a_{ol} = 4.75\,Å$ $b_{Hy} = b_{ol} = 10.2\,Å^{a}$ $c_{Hy} = 3c_{ol} = 18\,Å$ $V_{Hy} = 3V_{ol} = 873\,Å^{3}$ $Z = 12$ S.G. Pbnm $h_{Hy} + l_{Hy} \neq 2n + 1$

[a] b is assumed to be b_{ol}

Table 2 Calculated numbers of V''_{Me} vacancies in the olivine superstructures (Hy) estimated from SAED data

Olivine superstructure (Hy)	Ordered planar defects (PD)[a]		Calculated numbers of V''_{Me} vacancies[b]	
	Orientation	Periodicity	Averaged per one olivine unit cell	Per one olivine supercell (Hy)
Hy-2a	(1 0 0)	9.5 Å = $2a_{ol}$	1	2
Hy-3a	(1 0 0)	7.1 Å = $3/2a_{ol}$	4/3	4
Hy-3c	(0 0 1)	9 Å = $3/2c_{ol}$	4/3	4

[a] Planar defects (PD) are ordered in the olivine lattice

[b] Calculated from a model of planar defects with the M1 sites assumed to be completely vacant

structure. Again, sharp superspots should be observed in the diffraction pattern. (3) PD are fully M1-vacant but discontinuous. Diffraction patterns from Hy-3c (Fig. 7a), Hy-3a and Hy-2a (Fig. 7b) as well as the diffraction pattern from Hy-2a and Hy-3a (cf. Fig. 10 in Khisina et al. 2001) are consistent with both (1) and (2) models. In the model (3) the alternated layers of the PD-bearing structure and a normal olivine structure are expected. These alternated layers which are oriented normal to the PD plane should produce continuous streaks in a diffraction pattern. This case is observed in the Hy-3c superstructure in Fig. 7b.

The M1-vacancy concentrations per unit cell were calculated with the assumption that either all (Table 2) or half of the M1 positions in the planar defects are vacant. The data of Table 2 represent a maximum number of vacancies per unit cell, which is allowed for Hy-2a, Hy-3a and Hy-3c superstructures (all the M1 sites are vacant). If the M1 sites were only half-vacant, then the vacancy density would be halved compared to the data in Table 2. The resulted unit-cell geometries (Table 2) are in agreement with the space-group symmetry derived from SAED data (Table 1).

Hydrous olivine compositions

The olivine superstructures observed in both LI and SI of the olivine 9206 are interpreted as hydrous olivine with a composition of $Mg_{2-x}v_xSiO_4H_{2x}$ (Khisina et al., 2001). The reasons are: (1) OH-absorption bands have been observed in IR spectra of the olivine 9206 thus indicating the presence of water in the sample. (2) Hydrous phases like 10-Å phase, talc and serpentine have been observed in the olivine 9206, thus pointing out the extrinsic mode of hydrogen occurrence in the sample. (3) The OH-related prepeak at 528 eV was observed in the EEL spectra of LI and SI, thus indicating the presence of OH in LI and SI. (4) Both Fe/Si and Mg/Si ratio decrease in SI and LI with respect to the olivine matrix.

Metal vacancies in a defect olivine structure should be associated with either ferric iron or hydrogen or both of them to achieve charge neutrality: $[Fe^{\bullet}_{Me}] = 2[V''_{Me}]$, $[H_{Me}] = 2[V''_{Me}]$ and $[Fe^{\bullet}_{Me}] = [H_{Me}]$ (Mei and Kohlstedt 2000). Therefore, it is necessary to take ferric iron and hydrogen into account to derive a composition, which is equivalent to hydrous olivine. Unfortunately, it is not possible to discriminate Fe^{3+} and OH^- from EEL spectra (Fig. 4), because the prepeak at 528 eV, which is observed in the spectra of the inclusions, is indicative for both OH (Wirth 1997) and for Fe^{3+} (van Aken 1998).

The only possibility to discriminate the point-defect associates such as $[(OH)^{\bullet}_{O} - V''_{Me} - (OH)^{\bullet}_{O}]^{\leftrightarrow}$, $(Fe^{\bullet}_{Fe} - H'_{Me})^{\leftrightarrow}$ and $(2Fe^{\bullet}_{Fe} - V''_{Me})^{\leftrightarrow}$ in the inclusions is: (1) to calculate the cation composition in dependence on the point defect chemistry for the olivine with a given population of M1 vacancies and (2) to compare the result with the data observed. AEM measurements show that the iron concentration decreases in inclusions with respect to the iron concentration of the host olivine Fo_{92} (Fig. 2). We transformed the experimental net intensity ratio into atomic ratio data using the following procedure.

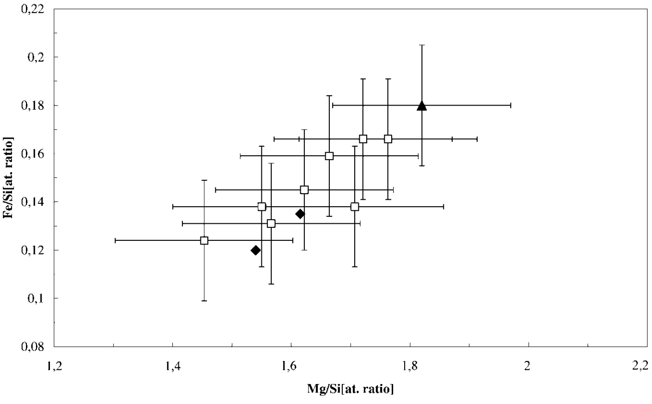

Fig. 8 Mg/Si atomic ratio versus Fe/Si atomic ratio. The *closed triangle* represents the measured values for olivine. *Open symbols* represent data of olivine matrix plus inclusions. The *two rectangular symbols* are the calculated ratios of hydrous olivine Hy-2a, Hy-3a and Hy-3c using a crystal-chemical approach (cf. text)

The relative elemental atomic concentrations (C_1 and C_2) and the corresponding c_1/c_2 concentration ratios in a specimen are directly calculated from the ratio of their X-ray intensities (I_1 and I_2):

$$\frac{C_1}{C_2} = k_{1,2}\frac{I_1}{I_2} \ , \tag{1}$$

where $k_{1,2}$ is a constant that accounts for the relative detection efficiency of the whole analysis system for the two elements. $k_{1,2}$ is easily deduced from a thin standard having a well-known proportion of the elements 1 and 2 (Chandler 1977). The C_1/C_2 concentration ratio is expressed in the form:

$$C_1/C_2 = (N_1/N_2)(W_1/W_2) \ , \tag{2}$$

where N_1/N_2 is the atomic ratio, W is atomic weight. Using the olivine matrix 9206 as internal standard with known Fe/Si (0.18) and Mg/Si (1.82) atomic ratios, the $(W_{Si}/W_{Fe})k_{Fe,Si}$ and $(W_{Si}/W_{Mg})k_{Mg,Si}$ are determined from Eqs. (1) and (2): $(W_{Si}/W_{Fe})k_{Fe,Si} = 1.410$, $(W_{Si}/W_{Mg})k_{Mg,Si} = 0.692$. The experimental Fe/Si and Mg/Si net intensity ratios are transformed to the Fe/Si and Mg/Si atomic ratios using Eqs. (1) and (2).

The Mg/Si versus Fe/Si atomic ratios are plotted in Fig. 8. The criterion for the theoretical chemical composition that is most likely is as follows: both Mg/Si and Fe/Si atomic ratios in the theoretical chemical formula of hydrous olivine should be lower than that in the host olivine (Mg/Si = 1.82; Fe/Si = 0.18), and should be consistent with the AEM data obtained from inclusions (Fig. 8). The theoretical chemical compositions of hydrous olivine structures with a given M1-vacancy population assuming either $[(OH)^{\bullet}_{O} - V''_{Me} - (OH)^{\bullet}_{O}]^{\leftrightarrow}$ or $(Fe^{\bullet}_{Fe} - H'_{Me})^{\leftrightarrow}$ or $(2Fe^{\bullet}_{Fe} - V''_{Me})^{\leftrightarrow}$ point-defect associates were calculated (see Table 4). The calculations are based on the following assumption: (1) Each M2 site next to the M1 vacancy is occupied by either Fe^{3+} only or Mg only. (2) The periodicity and the space-group symmetry of the hydrous olivine structure are assumed to be the same as that observed from SAED data (Table 1). (3) M1-vacancy populations are assumed to be the same as that calculated above (Table 2). The theoretical chemical composition of hydrous olivine was calculated for two cases assuming that the point-defect associates occur in either Fo_{100} or Fo_{92} olivine structure. Two models were treated: (1) point-defect associates in Fo_{92} olivine structure and (2) point-defect associates in Fo_{100} olivine structure. The reason for treating both models is the following. Model (1) is based on an assumption that the PD occurs within the olivine structure of the same composition, like that of the enclosing olivine matrix 9206 (Fo_{92}). On the other hand, according to the experimental data by McCammon et al. (1999), the oxidation state of iron in hydrous silicate phases is Fe^{3+}. Using these data (McCammon et al. 1999), we have to assume that the iron, if it is present, exists as Fe^{3+} in the inclusions. Therefore, the model (2) of PD in Fo_{100} olivine structure was used.

Table 3 Cation-deficient olivine compositions calculated in terms of the different point defect associates

Olivine superstructure (Hy)	Point-defect associate	Cation-deficient composition	Mg/Si	Fe/Si
Model 1. Point defect associates in forsterite, Fo_{100}				
Hy-2a	$\{V''_{Me}, 2(OH)^{\langle}\}$	$Mg_{1.75}v_{0.25}SiO_4H_{0.5}$	1.75	0
	$\left\{Fe^{\langle}_{Me}, H'_{Me}\right\}$	$Mg_{1.5}Fe^{3+}_{0.25}v_{0.25}SiO_4H_{0.25}$	1.5	0.25
	$\left\{2Fe^{\langle}_{Me}, V''_{Me}\right\}$	$Mg_{1.25}Fe^{3+}_{0.50}v_{0.25}SiO_4$	1.25	0.3
Hy-3a, Hy-3c	$\{V''_{Me}, 2(OH)^{\langle}\}$	$Mg_{1.66}v_{0.33}SiO_4H_{0.66}$	1.66	0
	$\left\{Fe^{\langle}_{Me}, H'_{Me}\right\}$	$Mg_{1.33}Fe^{3+}_{0.33}v_{0.33}SiO_4H_{0.33}$	1.33	0.33
	$\left\{2Fe^{\langle}_{Me}, V''_{Me}\right\}$	$Mg_{1.0}Fe^{3+}_{0.66}v_{0.33}SiO_4$	1.0	0.66
Model 2. Point-defect associates in Fo_{92}				
Hy-2a	$\{V''_{Me}, 2(OH)^{\langle}\}$	$Mg_{1.615}v_{0.25}Fe^{2+}{}_{0.135}SiO_4H_{0.5}$	1.615	0.135
	$\{Fe^{\langle}_{Me}, H'_{Me}\}$	$Mg_{1.365}Fe^{3+}_{0.25}v_{0.25}Fe^{2+}_{0.135}SiO_4H_{0.25}$	1.365	0.385
	$\{2Fe^{\langle}_{Me}, V''_{Me}\}$	$Mg_{1.13}Fe^{3+}_{0.50}v_{0.25}Fe^{2+}_{0.11}SiO_4$	1.13	0.61
Hy-3a, Hy-3c	$\{V''_{Me}, 2(OH)^{\langle}\}$	$Mg_{1.54}v_{0.33}Fe^{2+}_{0.12}SiO_4H_{0.66}$	1.54	0.12
	$\{Fe^{\langle}_{Me}, H'_{Me}\}$	$Mg_{1.215}Fe^{3+}_{0.33}v_{0.33}Fe^{2+}_{0.125}SiO_4H_{0.33}$	1.215	0.455
	$\{2Fe^{\langle}_{Me}, V''_{Me}\}$	$Mg_{0.91}Fe^{3+}_{0.66}v_{0.33}Fe^{2+}_{0.09}SiO_4$	0.91	0.75

Table 4 Unit cell parameters of hydrous olivine and corresponding chemical compositions derived from the experimental data using crystal chemical approaches

Hydrous olivine	Unit-cell parameters	Chemical composition (present data)	Extended crystal chemical formula
Hy-2a	a = 9.5 Å b = 10.2 Å[a] c = 6 Å V = 582 Å^3 Z = 8 Sp.G. P11 m or P1	$Mg_{1.615}Fe^{2+}_{0.135}v_{0.25}SiO_4H_{0.5}$ $= (Mg_{0.92}Fe_{0.08})_{1.75}v_{0.25}SiO_4H_{0.5}$ $= [MgSiO_4H_2] \cdot 3\ [Mg_{1.82}Fe_{0.18}SiO_4]$	
Hy-3a	a = 14.2 Å b = 10.2 Å[a] c = 6 Å V = 873 Å^3 Z = 12 Sp.G. Pbnm	$Mg_{1.54}Fe^{2+}_{0.12}v_{0.33}SiO_4H_{0.66}$ $= (Mg_{0.93}Fe_{0.07})_{1.66}v_{0.33}SiO_4H_{0.66}$ $= [MgSiO_4H_2] \cdot 2\ [Mg_{1.82}Fe_{0.18}SiO_4]$	$(Mg,Fe^{2+})_{2-x}v_xSiO_4H_{2x}$ $= [MgSiO_4H_2] \cdot n[(Mg,Fe^{2+})_2SiO_4]$ where $n = (1-x)/x$
Hy-3c	a = 4.75 Å b = 10.2 Å[a] c = 18 Å V = 873 Å^3 Z = 12 Sp.G. Pbnm	$Mg_{1.54}Fe^{2+}_{0.12}v_{0.33}SiO_4H_{0.66}$ $= (Mg_{0.93}Fe_{0.07})_{1.66}v_{0.33}SiO_4H_{0.66}$ $= [MgSiO_4H_2] \cdot 2\ [Mg_{1.82}Fe_{0.18}SiO_4]$	

[a] b_{Hy} assumed to be equal to b_{ol}

The theoretical chemical compositions of hydrous olivine calculated with the assumption that the PD occur in either Fo_{92} or Fo_{100} olivine structures, are listed in Table 3. The data show that neither $(Fe^{\langle}_{Fe} - H'_{Me})^{\leftrightarrow}$ nor $(2Fe^{\langle}_{Fe} - V''_{Me})^{\leftrightarrow}$ as point-defect associates can be present in Hy-2a, Hy-3a and Hy-3c because they would increase the Fe/Si ratio. The conditions of both Mg/Si and Fe/Si ratio to be lower than 1.82 and 0.18 are fulfilled only for $[(OH)^{\langle}_{O} - V''_{Me} - (OH)^{\langle}_{O}]^{\leftrightarrow}$ as a point-defect model (Table 3). The point defect associates $[(OH)^{\langle}_{O} - V''_{Me} - (OH)^{\langle}_{O}]^{\leftrightarrow}$ in Fo_{100} would result in compositions of Hy-2a, Hy-3a and Hy-3c, which would not be in agreement with the measured data in Fig. 8. However, in the case of Fo_{92}, the theoretical compositions are in good agreement with the measured chemical compositions (Fig. 8). The composition of Hy-2a is estimated to be $Mg_{1.615}\ Fe^{2+}_{0.135}v_{0.25}SiO_4H_{0.5}$, that of Hy-3a and Hy-3c is $Mg_{1.54}\ Fe^{2+}_{0.12}v_{0.33}SiO_4H_{0.66}$ (Tables 3, 4).

The modular structure of hydrous olivine

The crystal structure of hydrous olivine is proposed to be a modular olivine structure with Mg-vacant modules, which have a composition of $MgSiO_4H_2$ (see Fig. 9).

M1 vacancies in a given (1 0 0) octahedral layer of Hy-2a and Hy-3a structures alternate with occupied M2

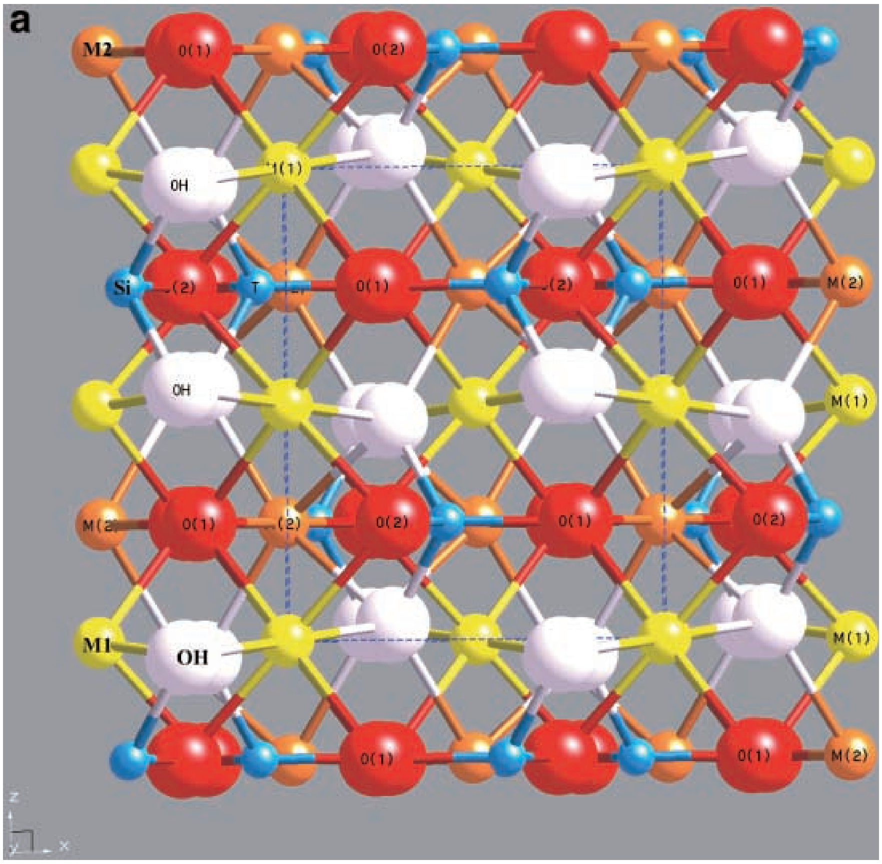

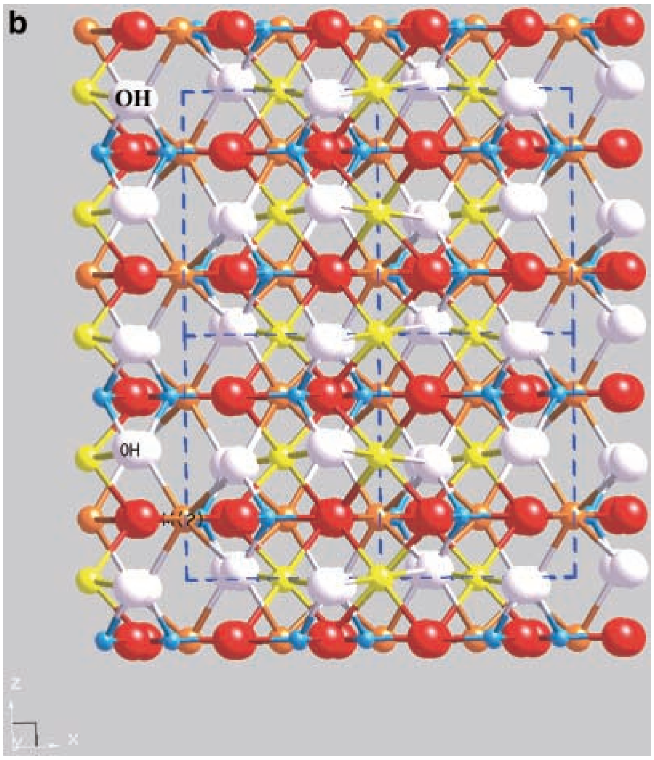

Fig. 9a–d The structure of olivine Mg_2SiO_4 projected along [0 1 0] **a.** **b**, **c** and **d** Sections of the three distinct olivine superstructures with M1-vacant modules. **b** and **c** Hy-2a and Hy-3a superstructures correspondingly. The (1 0 0) planar defects with 2a spacing in Hy-2a and with 3a spacing in Hy-3c are shown. Each of the M1 vacancies is connected to occupied M2 octahedra, thus forming $MgSiO_4H_2$ modules parallel to (1 0 0). **c** Hy-3c superstructure contains the (0 0 1) planar defects with 3c spacing. Each of M1 octahedra in a given (0 0 1) plane is vacant, thus forming $MgSiO_4H_2$ modules parallel to (0 0 1)

octahedra, while in the Hy-3c superstructure the M1 vacancies form the (0 0 1) octahedral layers which are free of cations. The crystal-chemical formula of hydrous olivine in terms of a modular structure can be written as $[MgSiO_4H_2] \cdot 3[Mg_{1.82}Fe_{0.18}SiO_4]$ for Hy-2a, as $[MgSiO_4H_2] \cdot 2[Mg_{1.82}Fe_{0.18}SiO_4]$ for Hy-3a and Hy-3c. The derived chemical compositions and unit-cell parameters of hydrous olivines are given in Table 4.

Fig. 9a–d (Continued)

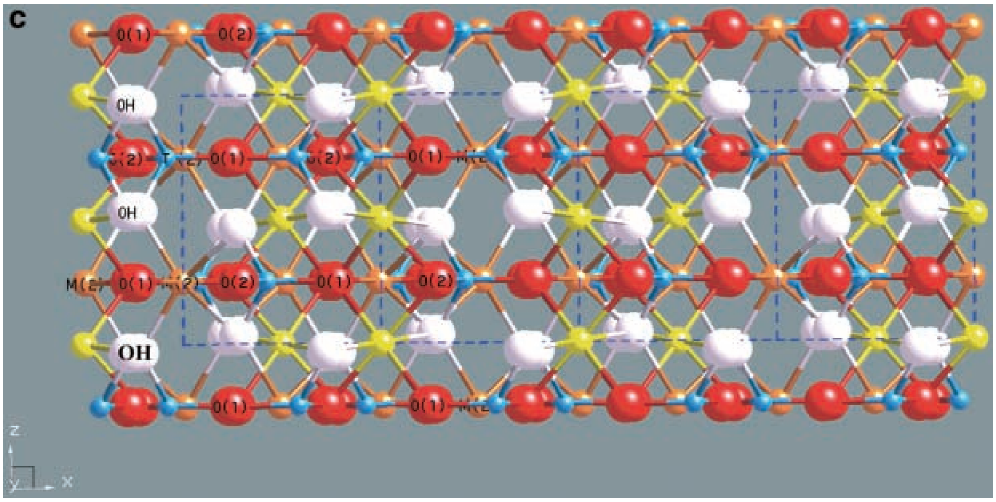

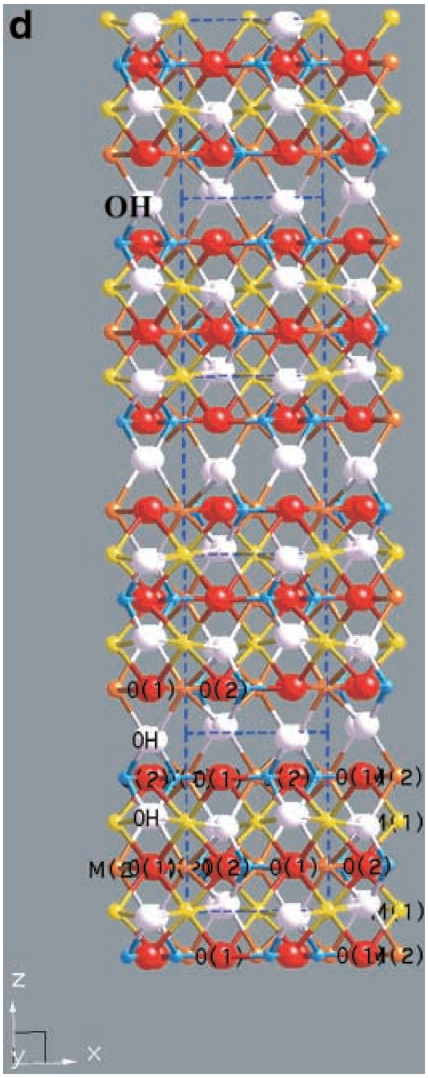

Discussion

Hydrous olivine is an example of a non-stochiometric compound with the point-defect concentration depending on the partial vapour pressure of the volatiles (oxygen, sulphur, water etc.). It is rather typical for non-stoichiometric compounds to arrange the vacancies with decreasing temperature in some kind of an ordered structure. There are many examples of such a mineral behaviour: cation-depleted wüstite $Fe_{1-x}O$, maghemite $Fe_{3-x}O_4$, laihunite $Fe_{2-x}SiO_4$, pyrrhotite $Fe_{1-x}S$. Planar defects which contain oxygen vacancies are known as Wadsley defects (Putnis 1992). It is interesting that even small changes in stoichiometry of the Wadsley defect-bearing structures are accommodated by changing the spacing and orientation of the Wadsley defects (Putnis 1992). With increasing deviation from stoichiometry, the defects become ordered into a parallel set with constant spacing. The ordered array of planar Wadsley defects produces a superlattice in which the periodicity of the basic cell is modified by the superimposed periodicity of the planar defects (Putnis 1992). Obviously, the planar defects in hydrous olivine have features in common with Wadsley defects. Wadsley defects are not very common in mineral structures. However, single as well as periodic or non-periodic planar defects in olivines are well known (Kondoh et al. 1985; Kitamura et al. 1985, 1987; Banfield et al. 1990, 1992; Khisina et al. 1995). (0 0 1) planar defects associated with OH groups have been observed in a mantle olivine by Kitamura et al. 1987. (0 0 1) planar defects associated with Fe^{3+} have been found in oxidised fayalites; these planar defects result in a crystal structure of laihunite $Fe_{1.0}v_{0.5}(Fe^{3+})_{0.5}SiO_4$ (Tamada et al. 1983). M1 sites in the average laihunite structure are occupied by vacancies and Fe^{2+} in alternating layers parallel to (0 0 1), while the M2 sites are predominately occupied by Fe^{3+} (Tamada et al. 1983; Shen et al. 1986). One-layer, two-layer and three-layer polytypes have been identified (cf. references in Kondoh et al. 1985). A three-layer polytype (3M-laihunite) with two defect rows per unit cell was suggested for Fe-laihunite (Shen et al. 1986). Periodic and non-periodic (1 0 0) planar defects are also very common in oxidised Mg-rich olivines (Banfield et al. 1990, 1992; Khisina et al. 1995; Janney and Banfield 1998). These planar

Table 5 Powder diffraction data for phase D (Liu 1987) indexed using the Hy-2a unit cell

Hy-2a $[Mg(OH)_2 \cdot SiO_2] \cdot 3Mg_2SiO_4$ (present work)		Phase D $Mg(OH)_2 \cdot SiO_2$ (Liu 1987)
Calculated from the data presented here		Powder diffraction data
hkl	d_{hkl}(Å)	d_{hkl}(Å)
1 0 0	9.5	9.5
2 1 1	4.3	4.3
0 3 0	3.49	3.37
0 0 2	3.00	3.00
2 0 2	2.57	2.53
0 4 0	2.55	
6 0 0	1.61	1.61
2 0 4	1.452	1.496
0 0 4	1.522	
6 3 3	1.39	1.390

defects were interpreted as an intergrowth of olivine and laihunite-like layers (Banfield et al. 1990, 1992; Khisina et al. 1995). Later, a three-layer distorted olivine structure with one defect row per unit cell was proposed for a natural olivine sample, $Fo_{0.13}$ (Janney and Banfield 1998). Therefore, we conclude that the superstructures caused by a periodic arrangement of ordered planar defects are rather common for olivines.

From the point-defect model, which is consistent with the experimental data, it is concluded that the point defect associates $[(OH)_O^{\langle} - V''_{Me} - (OH)_O^{\langle}]^{\leftrightarrow}$ are present in hydrous olivine structures. These point defects are condensed into ordered planar defects, which are observed in HRTEM lattice-fringe images like the periodic band-like contrasts. The latter disappeared during exposure to the electron beam (Fig. 5). The OH-related prepeak in EEL spectra also disappeared, thus indicating that the hydrous olivine is dehydrated due to irradiation damage. At the same time, neither in the HREM image nor in the diffraction pattern was the formation of an amorphous phase observed. In contrast, after irradiation, a clear and undisturbed lattice-fringe image of $(2\ 0\ 0)_{ol}$ and $(0\ 0\ 2)_{ol}$ lattice fringes appeared. This is explained by a change in the type of point defects. Instead of point-defect associates $[(OH)_O^{\langle} - V''_{Me} - (OH)_O^{\langle}]^{\leftrightarrow}$, Schottky defects are created: $[(OH)_O^{\langle} - V''_{Me} - (OH)_O^{\langle}]^{\leftrightarrow} (V''_{Me} - V''_O)^{\leftrightarrow} + H_2O \uparrow$.

Finally, the Schottky defects became disordered in the olivine lattice and therefore the superperiodicity disappeared. After irradiation, the olivine lattice inside inclusions represents a stoichiometric defect olivine structure saturated by vacancies in both M sites and oxygen sites. This phenomenon is well known in superconductors – compounds with a defect crystal lattice, which are described as either incommensurate or commensurate modulated structures (Withers and Rozier 2000).

Hydrous olivine $(Mg_{1-y}Fe^{2+}_y)_{2-x}v_xSiO_4H_{2x}$ has a modular structure and discrete composition with x values 0.33 or 0.25. Such a feature is typical for polysomatic series (Veblen 1991). Therefore, we consider hydrous olivines to be an intermediate member of the polysomatic series between olivine $(Mg, Fe)_2SiO_4$ and hypothetical $MgSiO_4H_2$. Hydrous olivine seems to be similar to the polysomatic series of humite-like minerals and polysomatic series of laihunites (Veblen 1991). The compositions of hydrous olivine, which are written as crystal-chemical formulas of modular compounds, are given in Table 4.

There is an interesting analogy between our data on hydrous olivine and data on some DHMS phases published by Kudoh and Inoue (1999) and Liu (1987). Kudoh et al. (1999) have synthesised hydrous wadsleyite $Mg_{2-x}SiO_4H_{2x}$ with $0 \geq x \leq 0.25$ and found that the crystal structure of $Mg_{1.75}SiO_4H_{0.5}$ contains Mg-vacant modules. These data on hydrous wadsleyite are similar to our interpretation of Hy-2a hydrous olivine, a composition which can be represented by $(Mg_{1-y}Fe^{2+}_y)_{1.75}$ $v_{0.25}SiO_4H_{0.5}$ (Table 4).

Liu (1987) has synthesised a DHMS phase with a calculated composition $MgSiO_4H_2$ and called this phase D. However, later it was assumed that Liu had obtained in his high-pressure–high-temperature experiments a mixture of several phases. Consequently, phase D by Liu was discredited (Yang et al. 1997). Now, phase D is used to describe the DHMS phase $MgSi_2H_2O_6$ (Yang et al. 1997). The powder diffraction pattern reported by Liu (1987) could never be indexed. However, the powder diffraction data given by Liu (1987) for phase D can be indexed in terms of hydrous olivine Hy-2a (Table 5). Phase D and the structural M1-vacant modules in our hydrous olivines are equivalent with respect to the chemical composition.

The question arises: what is the origin of hydrous olivine precipitates? From the observations it is obvious that hydrous olivine was precipitated from the olivine matrix, which initially was saturated in OH point defects, by an exsolution process. Based on the experimental study of water solution in the α, β and γ phases of $(Mg, Fe)_2SiO_4$ by Kohlstedt et al. (1996) – increasing water solubility with increasing pressure – we assume that olivine from nodule 9206 has been water-saturated under mantle conditions. The point-defect associates $(Fe_{Fe}^{\langle} - H'_{Me})^{\leftrightarrow}$ were estimated in olivine samples buffered near Ni/NiO (Mei and Kohlstedt 2000) but they are excluded in the mantle olivine 9206. This indicates that the olivine 9206 has been formed under oxygen fugacity conditions lower than Ni/NiO. Phase D by Liu, which is similar to Hy-2a, has been synthesised at 1000 °C at pressures exceeding 220 kbar (Liu 1987). Hence, we propose that the exsolution of hydrous olivine from the olivine matrix has occurred under high-pressure–high-temperature conditions. However, the pressure and temperature of hydrous olivine exsolution (like a transformation process) might have been lower than the *PT* conditions of synthesis of a pure phase. We suggest hydrous olivine to be a new DHMS phase(s) or, more precisely, a new DHMS polysomatic series.

Acknowledgements We would like to thank K. Paech for specimen preparation, and S. Churakov and B. Hein for technical assistance with the preparation of the manuscript. We thank W. Heinrich, V.S. Urusov, D. Price and J. Brodholt for their interest and useful comments. Discussions with A. Ul'yanov, Yu. Genshaft, V. Dritz, A.V. Sobolev and I. Veksler were constructive. The comments of an anonymous reviewer are gratefully acknowledged. The investigation was carried out with financial support of Russian Fond of Fundamental Research (99-05-65139 and 00-15-98582), Russian Federal Program Integration and INTAS Project 97-32174. The financial support of N.K. by the scientific visitor program of the GeoForschungsZentrum Potsdam GFZ is gratefully acknowledged.

References

Bai Q, Kohlstedt DL (1993) Effects of chemical environment on the solubility and incorporation mechanism for hydrogen in olivine. Phys Chem Miner 19: 460–471

Banfield JF, Veblen DR, Jones BF (1990) Transmission electron microscopy of subsolidus oxidation and weathering of olivine. Contrib Mineral Petrol 106: 110–123

Banfield JF, Diar MD, McGuire AV (1992) The defect microstructure of oxidised mantle olivine from Dish Hill, California. Am Mineral 77: 977–986

Beran A, Putnis A (1983) A model of the OH positions in olivine derived from infrared-spectroscopic investigations. Phys Chem Miner 9: 57–60

Brodholt JP (1997) Ab initio calculations on point defects in forsterite (Mg_2SiO_4) and implications for diffusion and creep. Am Mineral 82: 1049–1053

Brodholt JP, Refson K (2000) An ab initio study of hydrogen in forsterite and a possible mechanism for hydrolytic weakening. J Geophys Res 105: 18977–18982

Chandler JA (1977) X-ray microanalysis in the electron microscope. In: Glauert AM (ed) Practical methods in electron microscopy. North-Holland, Amsterdam

Janney DE, Banfield JF (1998) Distribution of cations and vacancies and the structure of the defects in oxidised intermediate olivine by atomistic-resolution TEM and image simulation. Am Mineral 83: 799–810

Khisina NR, Khramov DA, Kolosov MV, Kleschev AA, Taylor LA (1995) Formation of ferriolivine and magnesioferrite from Mg-Fe-olivine: reactions and kinetics of oxidation. Phys Chem Miner 22: 241–250

Khisina NR, Langer K, Andrut M, Ukhanov AV, Wirth R (2000) Nano-scale microstructure of Fe^{3+}-, OH^--bearing crystalline inclusions in experimentally oxidised olivine from a mantle nodule. Mineral Mag 64: 319–335

Khisina NR, Wirth R, Andrut M, Ukhanov AV (2001) Extrinsic and intrinsic mode of hydrogen occurrence in natural olivines: FTIR and TEM investigation. Phys Chem Miner 28: 291–301

Kitamura M, Shen B, Banno S, Morimoto N (1985) Fine texture of laihunite, a nonstoichiometric distorted olivine-type mineral. Am Mineral 69: 154–160

Kitamura M, Kondoh S, Morimoto N, Miller G, Rossman GR, Putnis A (1987) Planar OH-bearing defects in mantle olivine. Nature 328: 143–145

Kohlstedt DL, Keppler H, Rubie DC (1996) Solubility of water in the α, β and γ phases of $(Mg, Fe)_2SiO_4$. Contrib Mineral Petrol 123: 345–357

Kondoh S, Kitamura M, Morimoto N (1985) Synthetic laihunite $v_x(Fe^{2+})_{2-3x}(Fe^{3+})_{2x}SiO_4$, an oxidation product of olivine. Am Mineral 70: 737–746

Kröger FA (1971) The chemistry of compound semiconductors. Solid state, ed. Jost W, 780p, Academic Press

Kudoh Y, Inoue T (1999) Mg-vacant structural modules and dilution of the symmetry of hydrous wadsleyite, β-$Mg_{2-x}SiH_{2x}O_4$ with $0.00 \le x \le 0.25$. Phys Chem Miner 26: 382–388

Kudoh Y, Inoue T, Arashi H (1996) Structure and crystal chemistry of hydrous wadsleyite, $Mg_{1.75}SiH_{0.5}$: possible hydrous magnesium silicate in the mantle transition zone. Phys Chem Miner 23: 461–469

Kudoh Y, Kuibayashi T, Mizobata H, Ohtani E (2000) Structure and cation disorder of hydrous ringwoodite, γ-$Mg_{1.89}Si_{0.98}$-$H_{0.30}O_4$. Phys Chem Miner 27: 474–479

Lasaga AC (1981) The atomistic basis of kinetics: defects in minerals. In: Lasaga Ac, Kirkpatrick RJ (eds) Reviews in Mineralogy, Mineralogical Society of America, vol 8. pp 261–317

Libowitzky E, Beran A (1995) OH defects in forsterite. Phys Chem Miner 22: 387–392

Liu L-G (1987) Effects of H_2O on the phase behaviour of the forsterite–enstatite system at high pressures and temperatures and implications for the Earth. Phys Earth Planet Inter, 49: 142–167

McCammon CA, Smyth JR, Lausten HMS, Ross NL (1999) Oxidation state of iron in hydrous silicate phases. EUG 10 European Union of Geoscience Conference abstracts, 4; 1; 653

Mei S, Kohlstedt DL (2000) Influence of water on plastic deformation of olivine aggregates 1. Diffusion creep regime. J Geophys Res 105: 21457–21469

Putnis A (1992) Introduction to mineral sciences. Cambridge University Press, Cambridge

Shen B, Tamada O, Kitamura M, Morimoto N (1986) Superstructure of laihunite-3M $v_{0.40}(Fe^{2+})_{0.80}(Fe^{3+})_{0.80}SiO_4$. Am Mineral 71: 1455–1460

Tamada O, Shen B, Morimoto N (1983) The crystal structure of laihunite $v_{0.40}(Fe^{2+})_{0.80}(Fe^{3+})_{0.80}SiO_4$ – nonstoichiometric olivine-type mineral. Mineral J 11: 382–391

Thompson AB (1992) Water in the Earth's upper mantle. Nature 358: 295–302

Ukhanov AV, Ryabchikov ID, Kharkiv AD (1988) Lithospheric mantle of the Yakutia kimberlite province in Russian. Nauka, Moscow, 286 pp

van Aken PA, Liebscher B, Styrsa VJ (1998) Core-level electron energy-loss spectra of minerals: pre-edge fine structures at the oxygen K-edge. Phys Chem Miner 25: 494–498

Veblen DR (1991) Polysomatism and polysomatic series: a review and applications. Am Mineral 76: 801–826

Wirth R (1997) Water in minerals detectable by electron energy-loss spectroscopy EELS. Phys Chem Miner 24: 561–568

Wirth R, Khisina NR (1998) OH-bearing crystalline inclusions in olivine from kimberlitic peridotite (Udachnaya-East, Yakutia). Suppl EOS Trans 79, 45: T32B–17

Withers RL, Rozier P (2000) An electron diffraction study of Cu ordering in $Cu_{2.33-x}V_4O_{11}$. Z Kristallogr 215: 688–692

Wright K, Catlow CRA (1994) A computer simulation study of OH defects in olivine. Phys Chem Miner 20: 515–518

Yang H, Prewitt CT, Frost DJ (1997) Crystal structure of the dense hydrous magnesium silicate, phase D. Am Mineral 82: 651–654